

A kilometer-scale asteroid inside Venus's orbit

W.-H. Ip^{1*}, B. T. Bolin^{2,3*,**}, F. J. Masci³, Q. Ye⁴, E. A. Kramer⁵, G. Helou³,
 T. Ahumada⁵, M. W. Coughlin^{2,6}, M. J. Graham², R. Walters², K. P. Deshmukh⁷,
 C. Fremling², Z.-Y. Lin¹, J. W. Milburn⁸, J. N. Purdum⁹, R. Quimby^{9,10},
 D. Bodewits¹¹, C.-K. Chang¹, C.-C. Ngeow¹, H. Tan¹, C. Zhai⁴, P. van Dokkum¹¹,
 M. Granvik^{12,13}, Y. Harikane^{14,15}, L. A. Mowla¹¹, K. B. Burdge², E. C. Bellm¹⁶,
 K. De², S. B. Cenko^{17,18}, C. M. Copperwheat¹⁹, R. Dekany⁸, D. A. Duev²,
 D. Hale⁸, M. M. Kasliwal², S. R. Kulkarni², T. Kupfer²⁰, A. Mahabal²,
 P. J. Mróz², J. D. Neill², R. Riddle⁸, H. Rodriguez⁸, E. Serabyn⁵, R. M. Smith⁸,
 J. Sollerman²¹, M. T. Soumagnac^{22,23}, J. Southworth¹⁷, L. Yan²

¹Inst. of Astr., NCU, Taiwan, ²Div. of Phys., Math. and Astr., CIT, Pasadena, CA,

³IPAC, CIT, Pasadena, CA, ⁴Dept. of Astr., University of Maryland, College Park, MD,

⁵JPL, CIT, Pasadena, CA, ⁶School of Phys. and Astr., UMN, Minneapolis, MN,

⁷Dept. of Eng., IIT Bombay, Powai, India, ⁸COO, Pasadena, CA,

⁹Dept. of Astr., SDSU, San Diego, CA, ¹⁰Kavli Inst., Univ. of Tokyo, Tokyo, Japan,

¹¹Phys. Dept., Leach Science Center, Auburn University, Auburn, AL,

¹¹Astr. Dept., Yale Univ., New Haven, CT, ¹²Dept. of Phys., Univ. of Helsinki, Finland

¹³Div. of Space Tech., Univ. of Tech. Kiruna, Sweden

¹⁴Dept. of Phys. and Astr., UCL, London, UK,

¹⁵NOAJ, Tokyo, Japan, ¹⁶Dept. of Astr., UW, Seattle, WA,

¹⁷Astrophys. Sci. Div., NASA GSFC, Greenbelt, MD,

¹⁸Joint Space-Science Inst., UMD, College Park, MD,

¹⁹Astrophys. Research Inst., LJMU, Liverpool, UK,

²⁰Kavli Inst., Univ. of California, Santa Barbara, CA,

²¹Dept. of Astr., Stockholm Univ., Stockholm, Sweden,

²²LBNL, Berkeley, CA, ²³Dept. of Particle Phys. and Astrophys., WIS, Rehovot, Israel

*These authors contributed equally to this work.

**To whom correspondence should be addressed; bbolin@caltech.edu

One-sentence summary

The discovery by the Zwicky Transient Facility of the first asteroid interior to the orbit Venus, 2020 AV₂, may imply an additional source of asteroids in the inner Solar System.

Abstract

Near-Earth asteroid population models predict the existence of asteroids located inside the orbit of Venus. However, despite searches up to the end of 2019, none have been found. Here we report the discovery by the Zwicky Transient Facility of the first known asteroid located inside of Venus' orbit, 2020 AV₂, possessing an aphelion distance of 0.65 au and ~ 2 km in size. While it is possible that 2020 AV₂ is the largest of its kind, we find that its discovery is surprising in the context of population models where the expected count is close to zero. If this discovery is not a statistical fluke, then 2020 AV₂ may come from a yet undiscovered source population of asteroids interior to Venus, and currently favored asteroid population models may need to be adjusted.

Main Text

Almost all 1 million known asteroids are exterior to Earth's orbit with only a fraction of a percent located entirely inside its orbit (1, 2). No asteroids have yet been directly observed that exist entirely within the orbit of Venus despite dynamical models extrapolated from the known population of asteroids that predict their existence in small numbers (3–5). Here we report the first discovery of an asteroid interior to the orbit of Venus, 2020 AV₂ (6), that was first detected by the Zwicky Transient Facility (ZTF) on the Samuel Oschin Telescope (7, 8) on 2020 January 4 in four separate 30 s *r*-band exposures and moving ~ 1 degree per day (Fig. 1A-B).

The initial detection of 2020 AV₂ was made in the evening twilight sky while it was ~ 40 degrees from the Sun in what we call the Twilight Survey (Fig. S1). Additional data obtained with the Spectral Energy Distribution Machine (SEDM) on the Palomar 60-inch telescope (9) on 2020 January 8 and the Kitt Peak Electron Multiplying CCD Demonstrator (KPED) mounted on the Kitt Peak 84-inch telescope (10) on 2020 January 9 confirmed this asteroid as having an aphelion distance of ~ 0.65 au. Follow-up data obtained by our team and other observers during 2020 January 4-23 confirmed its aphelion distance of 0.653817 ± 0.000825 , or within the 0.72 au perihelion distance of Venus at $\sim 80\text{-}\sigma$ significance, confirming the discovery of the first inner-Venus asteroid (Fig. 2).

Spectroscopic observations of 2020 AV₂ made using the Keck telescope on 2020 January 23 indicate a reddish surface corresponding to colors of $g-r = 0.65 \pm 0.02$ mag, $r-i = 0.23 \pm 0.01$ mag and an absorption band at ~ 900 nm corresponding to $i-z = 0.11 \pm 0.02$ mag (Fig. 3). These data favor a silicate S-type asteroid-like composition (11, 12) consistent with an origin from the inner Main Belt where S-type asteroids are the most plentiful (13) and in agreement with the expectations of near-Earth asteroid (NEA) models that predict asteroids with the orbital elements of 2020 AV₂ (Tab. S1, Fig. S2) should originate from the inner Main Belt (5, 14). Such models also predict that 2020 AV₂ will have a surface reflectivity of $\sim 22\%$ (15–17). If so, 2020 AV₂ has a size of $\sim 1.5 \pm 0.5$ km with the main source of uncertainty resulting from measurements of its brightness. NEA population models predict < 1 inner-Venus asteroid of this size implying that 2020 AV₂ is one of the largest inner-Venus asteroids in the Solar System (5). In addition, dynamical N-body simulations of 2020 AV₂ indicate that its orbit is stable on ~ 10 Myr timescales, entering into temporary resonances with the terrestrial planets and Jupiter before its orbit evolves onto close-encounter paths with the gas giant leading to its eventual ejection from the Solar System (Fig. S3, see also refs. 18).

We estimated the number of inner-Venus asteroids expected to have been discovered by

ZTF by using synthetic inner-Venus asteroids generated by the NEA population model (Fig. 4, see also ref. 5) combined with ZTF’s completeness at recovering known asteroids during the ZTF survey (Figs. S1 and S4). The number of inner-Venus asteroids generated in our Synthetic population within a 68.2% confidence interval encompassing 2020 AV₂’s size is $0.29 \pm_{0.24}^{0.57}$ with the main source of uncertainty being from the estimate on 2020 AV₂’s size. The completeness of detecting inner-Venus asteroids is 0.18 ± 0.02 (Fig. 4), therefore, we expect $0.05 \pm_{0.04}^{0.09}$ inner-Venus asteroids to have been discovered during our observations. Despite its low probability, a possible explanation for our detection of 2020 AV₂ is a random chance discovery from the near-Earth asteroid population. However, history has shown that the first detection of a new class of objects is usually indicative of another source population c.f., such as the Kuiper Belt with the discovery of the first Kuiper Belt Objects 1992 QB₁ and 1993 FW (19). Therefore, 2020 AV₂ could have originated from a source of asteroids located closer to the Sun, such as near the stability regions located inside the orbit of Mercury at ~ 0.1 - 0.2 au where large asteroids could have formed and survived on time scales of the age of the Solar System (20, 21).

Acknowledgements

Based on observations obtained with the Samuel Oschin Telescope 48-inch and the 60-inch Telescope at the Palomar Observatory as part of the Zwicky Transient Facility project. ZTF is supported by the National Science Foundation under Grant No. AST-1440341 and a collaboration including Caltech, IPAC, the Weizmann Institute for Science, the Oskar Klein Center at Stockholm University, the University of Maryland, the University of Washington, Deutsches Elektronen-Synchrotron and Humboldt University, Los Alamos National Laboratories, the TANGO Consortium of Taiwan, the University of Wisconsin at Milwaukee, and Lawrence Berkeley National Laboratories. Operations are conducted by COO, IPAC, and UW.

SED Machine is based upon work supported by the National Science Foundation under

Grant No. 1106171

The KPED team thanks the National Science Foundation and the National Optical Astronomical Observatory for making the Kitt Peak 2.1-m telescope available. We thank the observatory staff at Kitt Peak for their efforts to assist Robo-AO KP operations. The KPED team thanks the National Science Foundation, the National Optical Astronomical Observatory, the Caltech Space Innovation Council and the Murty family for support in the building and operation of KPED. In addition, they thank the CHIMERA project for use of the Electron Multiplying CCD (EMCCD).

The authors would like to thank Alessandro Morbidelli for useful discussion in the interpretation of the first inner-Venus asteroid discovery as well as providing the synthetic asteroid population used to model our survey efficiencies.

M. W. Coughlin acknowledges support from the National Science Foundation with grant number PHY-2010970.

C.F. gratefully acknowledges the support of his research by the Heising-Simons Foundation (#2018-0907).

Some of the data presented herein were obtained at the W. M. Keck Observatory, which is operated as a scientific partnership among the California Institute of Technology, the University of California and the National Aeronautics and Space Administration. The Observatory was made possible by the generous financial support of the W. M. Keck Foundation.

The authors wish to recognize and acknowledge the very significant cultural role and reverence that the summit of Maunakea has always had within the indigenous Hawaiian community. We are most fortunate to have the opportunity to conduct observations from this mountain.

This work has made use of data from the European Space Agency (ESA) mission *Gaia* (<https://www.cosmos.esa.int/gaia>), processed by the *Gaia* Data Processing and Analysis Consortium (DPAC, <https://www.cosmos.esa.int/web/gaia/dpac/>

consortium). Funding for the DPAC has been provided by national institutions, in particular the institutions participating in the *Gaia* Multilateral Agreement.

Authors Contributions

W.-H.I. helped initiate, design and secure P48 time for the ZTF Twilight. B.T.B. discovered 2020 AV₂ in the ZTF data and realized it had an orbit interior to Venus', led the study, wrote the manuscript, reviewed and scanned all candidate asteroid detections for the duration of this study, helped design and secure time for the Twilight survey and for follow-up, prepared and executed follow-up observations, reduced the photometric and spectroscopic data, did the astrometry, orbit determination, helped generate the synthetic NEA population, calculated the survey completeness and estimates of the inner-Venus asteroid population. F.J.M. served as the Science Data System Lead of the ZTF collaboration, wrote and maintained software for extraction of moving objects in ZTF data, calculated the survey completeness, maintained the ZTF data system, helped secure P48 time for the ZTF Twilight survey, helped design and initiate the Twilight survey. Q.Y. contributed code used to schedule the ZTF survey and contributed improvements to the moving object identification pipeline, and helped initiate and design the Twilight survey. E.K. monitored the NEA discovery performance of the ZTF survey. G.H. helped with the interpretation of the completeness calculation, helped prepare the manuscript, served as the Primary Investigator of the team observing NEAs with ZTF and as the Data Archive Director of the ZTF collaboration, helped design the cadence, secure P48 time for the ZTF Twilight survey and is one of its initiators. E.K. monitored the NEA discovery performance of the ZTF survey. G.H. served as the Primary Investigator of the team observing NEAs with ZTF and as the Data Archive Director of the ZTF collaboration, helped design the cadence, secure P48 time for the ZTF Twilight survey and is one of its initiators. E.K. monitored the NEA discovery performance of the ZTF survey. G.H. served as the Primary Investigator of the team observing

NEAs with ZTF and as the Data Archive Director of the ZTF collaboration, helped design the cadence, secure P48 time for the ZTF Twilight survey and is one of its initiators. T.A. and M.C. performed follow-up observations of 2020 AV₂ with KPED and contributed to the reduction of photometry. M.G. served as the Project Scientist of ZTF, secured time with Keck I and took spectroscopic observations of 2020 AV₂ with Keck I/LRIS and reduced spectral data. R.W. performed follow-up observations of 2020 AV₂ with SEDM. K.P.D. contributed to planning follow-up observations of 2020 AV₂. C.F. contributed to the planning of spectroscopy observations of 2020 AV₂ with Keck and spectroscopic data reduction. Z.-Y.L. contributed to the interpretation of the 2020 AV₂ spectroscopy data. J.W.M. contributed to follow-up observations of 2020 AV₂. J.P. and R.Q. contributed to the reduction of photometry and follow-up observations of 2020 AV₂. C.-K.C., C.-C.N. and H.T. contributed to securing time with the P48 for ZTF Solar System observations. C.Z., C.M.C and J.S. were members of the team that conducts follow-up observations of ZTF Solar System discoveries. P.D. and L.A.M. helped secure time for follow-up observations of 2020 AV₂. M.G. helped generate the synthetic NEA population. K.B.B. and K.D. contributed to the reduction of Keck/LRIS spectroscopy data of 2020 AV₂. E.C.B. served as the Survey Scientist of the ZTF collaboration and scheduled the observations taken with the P48 during the ZTF Twilight survey. S.B.C. contributed to the planning of P48 time used in the Twilight survey. D.A.D, A.M. and P.J.M. wrote and maintained software and machine learning algorithms for the ZTF data pipeline and identification of sources in ZTF data. A.M. served as the Machine Learning Lead for the ZTF collaboration. R.D. served as the Project Manager of the ZTF collaboration and contributed to the design and construction of the ZTF camera. D.H. contributed to the design and construction of the ZTF camera. M.K. served as the Primary Investigator of the Global Relay of Observatories Watching Transients Happen (GROWTH) team for follow-up of ZTF discoveries. S.R.K. served as the Principal Investigator of the ZTF collaboration and survey. T.K. and M.T.S. contributed to the ZTF cali-

bration pipeline. J.D.N. contributed to SEDM operations and observations of 2020 AV₂. R.R. contributed to maintaining ZTF operations. H.R. contributed to SEDM operations. E.S. contributed to KPED operations and observations of 2020 AV₂. R.M.S. served as the Lead Camera Engineer for the ZTF survey and lead the design and construction of the ZTF camera. J.S. contributed to SEDM operations and observations of 2020 AV₂. L.Y. contributed to planning and securing of telescope time for follow-up observations of 2020 AV₂.

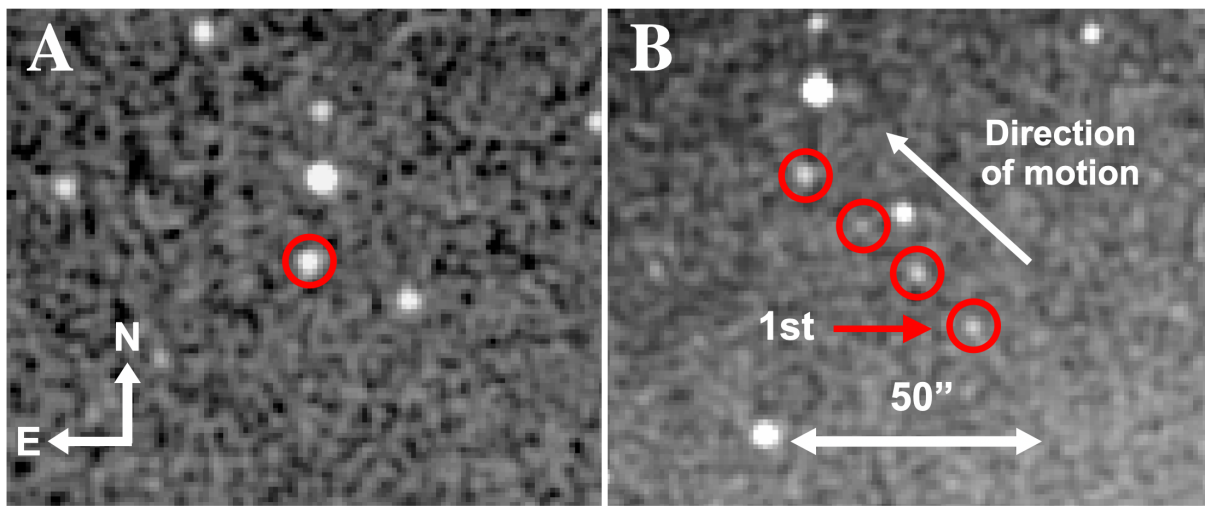


Figure 1: (A) Discovery 30 s r-band image of 2020 AV₂ taken on 2020 January 4 UTC where 2020 AV₂ is the detection located in the circle. (B) Composite image containing the four discovery 30 s r-band exposures covering 2020 AV₂ made by stack on the rest frame of the background star over a 22 minute time interval. The first detection has been labeled. The asteroid was moving ~ 1 degree per day in the northeast direction while these images were being taken resulting in a ~ 15 arcseconds spacing between the detections of 2020 AV₂. The cardinal directions and spatial scale are indicated for reference.

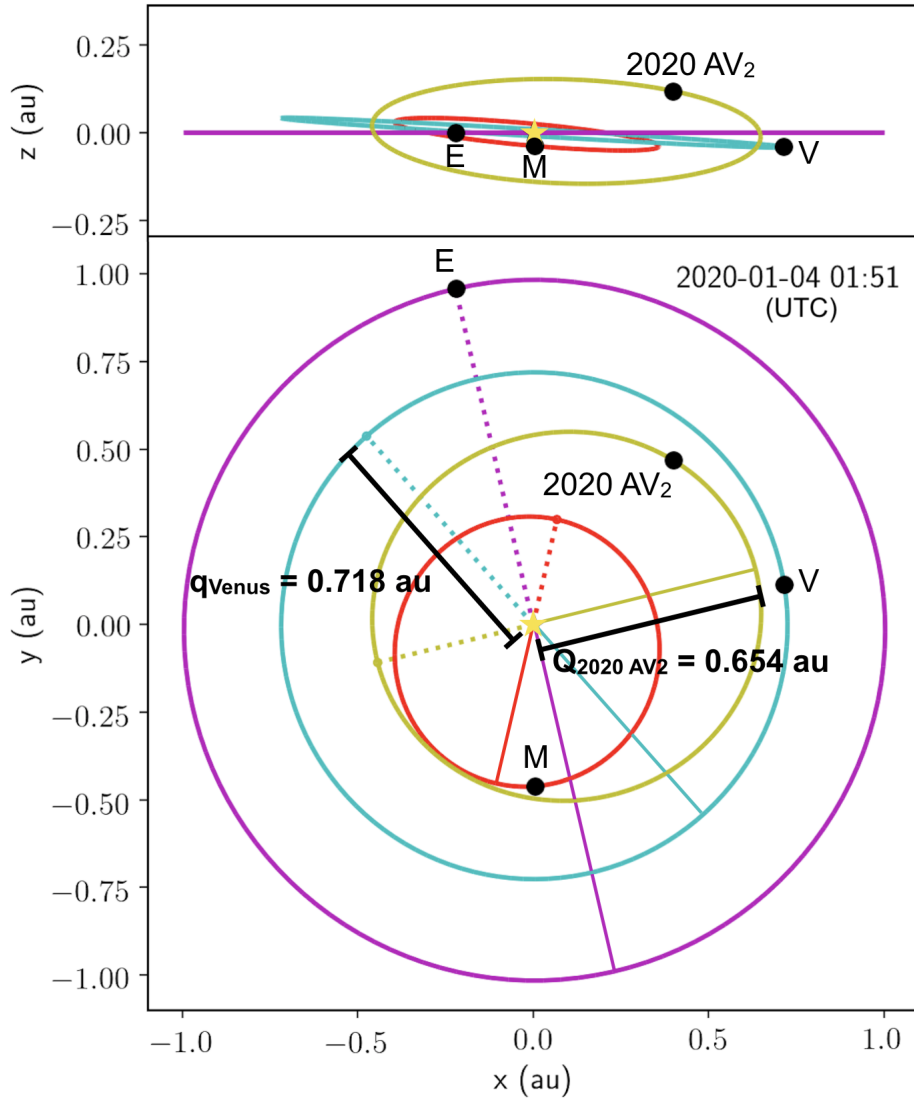


Figure 2: Orbital configuration of 2020 AV₂, Earth, Venus and Mercury at the time of 2020 AV₂'s discovery looking from above the orbital plane of the inner Solar System. The orbit plotted for 2020 AV₂ in this figure is taken from the orbital elements in Tab. S1. The perihelion directions of 2020 AV₂ and the planets are plotted with dotted lines. The aphelion directions of 2020 AV₂ and the planets are plotted with solid straight lines.

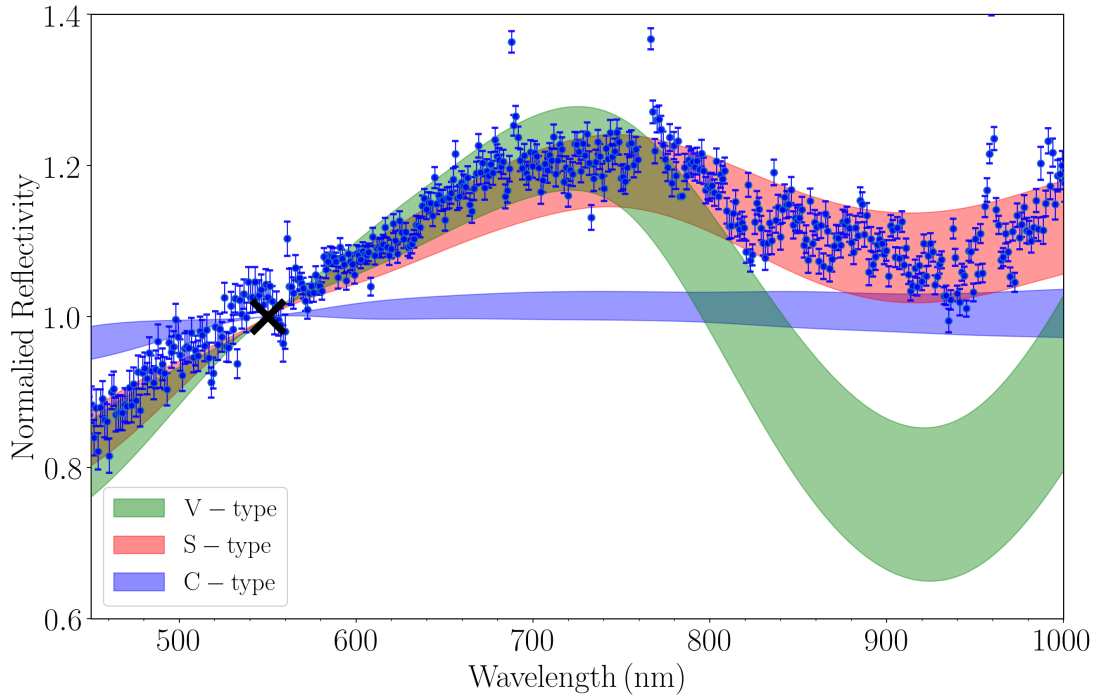


Figure 3: Visible wavelength reflectance spectrum taken of 2020 AV₂ with the LRIS instrument on Keck I on 2020 January 23 plotted as blue dots. The error bars on the spectrum data points correspond to 1- σ uncertainty. The spectrum has been normalized to unity at 550 nm indicated by the black cross. The spectrum presented was obtained by combining two spectra from the blue camera using the 600/4000 grating and the red camera using the 400/8500 grating with a 560 nm dichroic (22, 23). The data have been rebinned and smoothed by a factor of 10 using an error-weighted mean. The spectral range of S, V and C-type asteroids from the Bus-DeMeo asteroid taxonomic catalogue (12) are over-plotted with the S-type spectrum most closely resembling the spectra of 2020 AV₂.

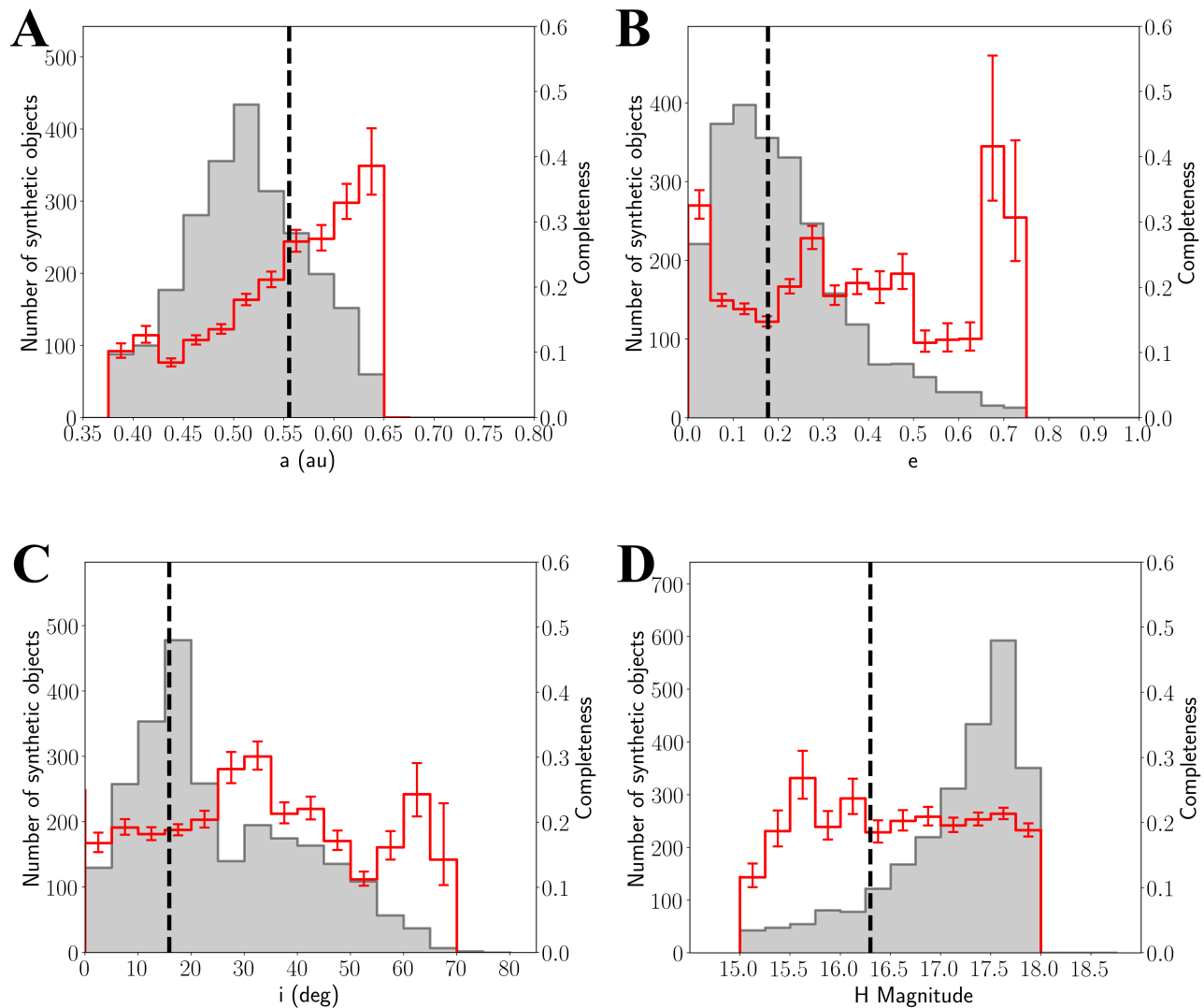


Figure 4: Comparison between the (A) semi-major axis, a , (B) eccentricity, e , (C) inclination i and (D) absolute magnitude H distribution of the number of synthetic inner-Venus asteroids generated from the NEA model (5) (grey histograms) and the completeness of synthetic inner-Venus asteroids detected in the survey simulation (red histogram). The 1- σ error bars on the completeness are determined assuming Poissonian statistics. The vertical dashed black line indicates the value of the element for 2020 AV₂ from Tab. S1. The absolute magnitude range of 15 to 18 corresponds to asteroids in the size range of ~ 1 -3 km assuming a 20% surface reflectivity. The number of objects from the NEA model has been oversampled by a factor of 1,000.

References and Notes

1. R. P. Binzel, V. Reddy, T. L. Dunn, *The Near-Earth Object Population: Connections to Comets, Main-Belt Asteroids, and Meteorites* (2015), pp. 243–256.
2. R. Jedicke, *et al.*, *Surveys, Astrometric Follow-Up, and Population Statistics* (2015), pp. 795–813.
3. G. W. Wetherill, *Icarus* **37**, 96 (1979).
4. P. Michel, V. Zappalà, A. Cellino, P. Tanga, *Icarus* **143**, 421 (2000).
5. M. Granvik, *et al.*, *Icarus* **312**, 181 (2018).
6. B. T. Bolin, *et al.*, *Minor Planet Electronic Circulars* **2020-A99** (2020).
7. E. C. Bellm, *et al.*, *Publications of the Astronomical Society of the Pacific* **131**, 018002 (2019).
8. M. J. Graham, *et al.*, *Publications of the Astronomical Society of the Pacific* **131**, 078001 (2019).
9. N. Blagorodnova, *et al.*, *Publications of the Astronomical Society of the Pacific* **130**, 035003 (2018).
10. M. W. Coughlin, *et al.*, *Monthly Notices of the Royal Astronomical Society* **485**, 1412 (2019).
11. S. J. Bus, R. P. Binzel, *Icarus* **158**, 146 (2002).
12. F. E. DeMeo, R. P. Binzel, S. M. Slivan, S. J. Bus, *Icarus* **202**, 160 (2009).
13. F. E. DeMeo, B. Carry, *Nature* **505**, 629 (2014).

14. M. Granvik, *et al.*, *Nature* **530**, 303 (2016).
15. F. E. DeMeo, B. Carry, *Icarus* **226**, 723 (2013).
16. R. P. Binzel, *et al.*, *Icarus* **324**, 41 (2019).
17. A. Morbidelli, *et al.*, *Icarus* **340**, 113631 (2020).
18. S. Greenstreet, *Monthly Notices of the Royal Astronomical Society* (2020).
19. D. Jewitt, J. Luu, *Nature* **362**, 730 (1993).
20. N. W. Evans, S. Tabachnik, *Nature* **399**, 41 (1999).
21. A. Shannon, A. P. Jackson, D. Veras, M. Wyatt, *Monthly Notices of the Royal Astronomical Society* **446**, 2059 (2015).
22. J. B. Oke, *et al.*, *Publications of the Astronomical Society of the Pacific* **107**, 375 (1995).
23. J. K. McCarthy, *et al.*, *Blue channel of the Keck low-resolution imaging spectrometer* (1998), vol. 3355 of *Society of Photo-Optical Instrumentation Engineers (SPIE) Conference Series*, pp. 81–92.
24. S. Keys, *et al.*, *Publications of the Astronomical Society of the Pacific* **131**, 064501 (2019).
25. E. C. Bellm, *et al.*, *Publications of the Astronomical Society of the Pacific* **131**, 068003 (2019).
26. F. J. Masci, *et al.*, *Publications of the Astronomical Society of the Pacific* **131**, 018003 (2019).
27. D. A. Duev, *et al.*, *Monthly Notices of the Royal Astronomical Society* **486**, 4158 (2019).
28. Q. Ye, *et al.*, *Astronomical Journal* **159**, 70 (2020).

29. R. Dekany, *et al.*, *Proceedings of SPIE* (2016), vol. 9908 of *Society of Photo-Optical Instrumentation Engineers (SPIE) Conference Series*, p. 99085M.
30. Q. Ye, *et al.*, *Publications of the Astronomical Society of the Pacific* **131** (2019).
31. M. Rigault, *et al.*, *Astronomy & Astrophysics* **627**, A115 (2019).
32. D. A. Perley, *Publications of the Astronomical Society of the Pacific* **131**, 084503 (2019).
33. Gaia Collaboration, *et al.*, *Astronomy & Astrophysics* **595**, A1 (2016).
34. Gaia Collaboration, *et al.*, *Astronomy & Astrophysics* **616**, A1 (2018).
35. H. Raab, *Astrometrica: Astrometric data reduction of CCD images* (2012).
36. K. C. Chambers, *et al.*, *ArXiv e-prints* (2016).
37. H. A. Flewelling, *et al.*, *ArXiv e-prints* (2016).
38. H. Rein, S.-F. Liu, *Astronomy & Astrophysics* **537**, A128 (2012).
39. H. Rein, D. S. Spiegel, *Monthly Notices of the Royal Astronomical Society* **446**, 1424 (2015).
40. D. Nesvorný, F. Roig, S. Ferraz-Mello, *Astronomical Journal* **119**, 953 (2000).
41. C. de la Fuente Marcos, R. de la Fuente Marcos, *Monthly Notices of the Royal Astronomical Society* **494**, L6 (2020).
42. M. Granvik, *et al.*, *Astronomy & Astrophysics* **598**, A52 (2017).
43. B. T. Bolin, M. Delbo, A. Morbidelli, K. J. Walsh, *Icarus* **282**, 290 (2017).

44. A. Morbidelli, R. Gonzi, C. Froeschle, P. Farinella, *Astronomy & Astrophysics* **282**, 955 (1994).
45. A. Milani, G. F. Gronchi, *Theory of Orbital Determination* (Cambridge University Press, 2010).
46. J. Wisdom, *Icarus* **56**, 51 (1983).
47. E. Bowell, *et al.*, *Asteroids II* pp. 399–433 (1988).
48. P. Vereš, *et al.*, *Icarus* **261**, 34 (2015).
49. R. Jedicke, B. Bolin, M. Granvik, E. Beshore, *Icarus* **266**, 173 (2016).
50. S. P. Naidu, S. R. Chesley, D. Farnocchia, *AAS/Division for Planetary Sciences Meeting Abstracts #49*, AAS/Division for Planetary Sciences Meeting Abstracts (2017), p. 112.04.

List of Supplementary Materials

Methods

Discovery, follow-up and orbital determination

Twilight Survey strategy

Discovery, follow-up and characterization observations

Visual imaging/spectroscopy reduction and astrometry

Dynamical evolution

Comparison with the NEA population

Estimating the ZTF inner-Venus asteroid population completeness

Figs. S1-S4

Tab. 1

References (24-50)

Supplementary Material

Methods

Discovery, follow-up and orbital determination: The initial discovery observations of 2020 AV₂ on 2020 January 4 were made in four sidereally-tracked 30 s r-band exposures by the 48-inch Samuel Oschin Telescope. The observations were made during evening astronomical twilight while the telescope was pointing at 25.5 degrees elevation and the center of the telescope's field of view was pointing through 2.3 airmasses. The brightness of 2020 AV₂ during its discovery observations were $r \sim 18.1$ and was moving approximately 0.85 degrees/day. The observations were taken during average seeing conditions for the Palomar site with nearby stellar objects of similar brightness to 2020 AV₂ having FWHM $\sim 2.1''$. The sky plane rate of motion

of 2020 AV₂ during the observations was 2.1"/min resulting in no significant trailing losses of the individual detections of 2020 AV₂ in the discovery images (Fig. 1, A-B).

The preliminary orbit of 2020 AV₂ determined from the discovery observations was first classified as an Apollo-like orbit based on the initial discovery observations with $a \sim 1.53$ au and eccentricity $e \sim 0.45$ with a near-Earth asteroid (NEA) digest2 score of 98 (24). After including the SEDM and KPED observations made on 2020 January 8 and 9, the semi-major axis became $a \sim 0.551 \text{ au} \pm 0.004$, eccentricity $e \sim 0.191 \pm 0.008$ resulting in an aphelion $Q \sim 0.657 \pm 0.001$ au. Additional observations taken by other groups up until January 23 later revised to $Q = 0.654 \pm 0.001$, a $>50\text{-}\sigma$ confidence interval smaller than the 0.72 au perihelion distance of Venus (Supplementary Material Tab. S1 and Fig. S2). No pre-discovery observations of 2020 AV₂ were located in the ZTF archive.

Twilight Survey strategy: Astronomical twilight time is used by ZTF to search for Solar System objects at small Solar elongations <60 degrees from the Sun in a program called the “Twilight Survey” during which 2020 AV₂ was discovered. Searching for Solar System objects so close to the Sun during twilight is accomplished by using the 47 sq. degree field of view and minimum elevation of the 48-inch Samuel Oschin Telescope to point the telescope as close to the horizon as possible during evening and morning Astronomical twilight when the Sun is ~ 18 degrees below the horizon (25). This results in being able to search the night sky to as close as ~ 35 degrees from the Sun, corresponding to potentially detecting objects as close as ~ 0.57 au from the Sun.

ZTF uses a nearly contiguous 10 field pattern when executing the Twilight Survey, providing ~ 470 square degrees of sky coverage per Twilight Survey session and covering an area of the sky with ~ 20 degrees elevation and airmass <2.9 in the evening and morning sky implemented by the ZTF survey scheduler (25). Each Twilight Survey session lasts 20-25 minutes where each field is imaged four times with 30 s exposures in r -band, resulting in a ~ 5 minute spacing

between exposures in each of the 10 fields. This allows for the positive identification of objects moving as slow as ~ 0.05 degrees/day to as fast as >10 degrees/day by the ZTF processing system (26, 27). The limiting magnitude in each of the 30 s r -band exposures is degraded due to the extinction at its higher airmass observations and higher sky background resulting in a limiting magnitude closer to $V \sim 20.6$ compared to the nominal ZTF limiting magnitude of $V \sim 21.2$ (7, 8).

The Twilight Survey that our results are based on began on 2019 September 20 and was based on an earlier version that ran during Winter 2018 and Summer 2019 (28). The current Twilight Survey is ongoing, but poor weather in February and March limits this analysis to survey dates between 2019 September 19 and 2020 January 30. The current Twilight Survey executes its 10 field coverage each night, weather-permitting, alternating between evening and morning twilight. The preliminary version of the Twilight Survey ran on a more sporadic cadence where it only operated on a 3-day cadence alternating between evening and morning twilight. We sought to improve our survey coverage and rate of self-recovery of candidate discoveries by moving to the current every night cadence. In total, the Twilight Survey was carried out 90 times between 2019 September 20 and 2020 January 30 split into 47 mornings and 43 evenings. The complete Sun-centered sky coverage of these 100 observing sessions is presented in Fig. S1. In total, $\sim 50,000$ square degrees of the sky was covered four times during the entirety of the Twilight Survey discussed in this analysis.

Discovery, follow-up and characterization observations:

Zwicky Transient Facility, ZTF: The ZTF camera consists of 16 separate 6144 x 6160-pixel arrays on a single CCD camera mounted on the 48-inch Samuel Oschin Telescope at Palomar Observatory and is robotically operated. The plate scale of the camera is 1.01 arcseconds/pixel and has a 7.4-degree x 7.4-degree field of view (7, 29). The data processing pipeline produced images differenced from reference frames and removes or masks most detector artifacts. Tran-

sient are extracted from the images and several algorithms are used to identify slower moving objects that appear as round PSF detections in the images (26) and to extract fast-moving objects that appear as streaked detections (27, 30). Moving objects can be identified in images taken in each of its g , r and i band filters. For the purpose of the Twilight Survey, 30 s exposures were used with the r filter. Seeing was measured to be ~ 2.1 arcsec of stars near the detection of 2020 AV₂ in the discovery images.

Spectral Energy Distribution Machine, SEDM: Observations taken by the SEDM used the Rainbow Camera consisting of two identical Princeton Instruments Pixis 2048B eXelon model 2048 x 2048 pixel CCDs mounted on the Palomar 60-inch telescope and is robotically operated (9, 31). The Rainbow Camera has a 13 arcminute x 13 arcminute field of view divided into four ~ 6 arcminute quadrants with each having coverage of a single filter, u , g , r and i and a 0.125 arcseconds/pixel spatial scale. Only the r filter quadrant was used for our follow-up observations with SEDM with non-sidereally tracked 30 s exposures. Seeing conditions were ~ 1.75 arcsec as measured for background stars in the follow-up images.

Kitt Peak Electron Multiplying CCD Demonstrator, KPED: The KPED instrument is mounted on the Kitt Peak 84-inch telescope and consists of a 1024 x 1024 pixel Electron Multiplying CCD camera and is robotically operated (10). The camera has a spatial scale of 0.26 arcseconds/pixel and a 4.4 arcminute x 4.4 arcminute field of view. The camera is capable of reading out at a rate of 1 Hz and of individual exposures times up to 10 s. Our observations used 10 s exposures in r -band and were sidereally tracked due to the short exposure time. Seeing conditions were ~ 1 arcsec as measured for background stars in the follow-up images.

Keck I Telescope: The Low Resolution Imaging Spectrometer (LRIS) (22) on the Keck I telescope was used to observe 2020 AV₂ on 2020 January 23 in spectroscopy mode (Program ID C272, PI M. Graham). Both the blue camera consisting of a 2 x 2K x 4K Marconi CCD array and the red camera consisting of a science grade Lawrence Berkeley National Laboratory

2K x 4K CCD array were used. Both cameras have a spatial resolution of 0.135 arcsec/pixel. The 1.0-arcsecond wide slit was used with the 560 nm dichroic with $\sim 50\%$ transmission efficiency in combination with the 600/4000 grating for the blue camera and the 400/8500 grating for the red camera providing a spectral resolution of 0.4 nm and 0.7 nm, respectively (22, 23). A total exposure time of 600 s over two integrations were taken in seeing conditions of ~ 0.6 arcseconds measured at zenith, however, the observations were taken at the large airmass of ~ 3.4 significantly degrading the seeing to ~ 1.2 arcsec. Wavelength calibration was completed using the HgCdZn lamps for the blue camera and the ArNeXe lamps for the red camera. Flux calibration was completed with the G191-B2B and Feige 34 standard stars for the blue and red camera respectively and a Solar analog 2MASS 22462446+0029244 was used to produce the reflectance spectrum as seen in (Fig. 3).

Visual imaging/spectroscopy reduction and astrometry: All visual imaging data was reduced using custom code for bias and flat field detrending. The LRIS spectroscopic data were reduced using flat field, dark current and arc lamp exposures with the LPipe spectroscopy reduction software (32). The *Gaia* data release 2 catalog (33, 34) was used with the ZTF data reduction pipeline (26) to produce an astrometric solution on ZTF data and with the Astrometrica software (35). Photometric calibration was performed using the Pan-STARRS1 catalog database (36, 37).

Dynamical evolution: We used the `rebound` N-body orbit integration package (38) using the `IAS15` adaptive time step integrator (39) to determine the orbital history of 2020 AV₂. Using the multi-variate distribution of the orbital parameters presented in Tab. S1 and Fig. S1, we integrated several 100 clone orbits of 2020 AV₂ forwards and backward 30 Myrs with a nominal timestep of 14 h. Because it is an adaptive time-step integrator, `IAS15` will decrease the time of this time step during close encounters to avoid discrepancies in the orbits of test particles resulting from too coarse time steps. We find that 2020 AV₂ has experienced numerous,

~ 0.01 au close encounters with Mercury and Venus that are as frequent as every few hundred to thousands of years.

One of the main features of the long term orbital evolution of 2020 AV₂ is its occasional capture into mean motion resonances with Venus such as the 3:2 mean motion resonance at $\sim 40,000$ y seen as in Fig. S3 (A) for the orbit of one particular clone. The amplitude of libration is initially large but dramatically shrinks after close encounters with Mercury after 50,000 y resulting in a correlation with an increase in the minimum approach distance to Venus as seen in Fig. S3 (B) protecting it from close encounters with the planet similar to the effect of the 2:3 mean motion resonances between Neptune and Pluto protecting the latter from encounters with the former (40). At the precision of the current orbit, 2020 AV₂ will remain in resonance with Venus for ~ 1 Myr, though subsequent observations of 2020 AV₂ during its next apparition in the fall of 2020 may improve the orbital accuracy to allow for longer-term investigation of this resonant behavior (18, 41). In any case, the orbit of 2020 AV₂ is firmly confined within the orbit of Venus with having an aphelion distance of < 0.72 au for the majority of its orbital evolution for the previous and next 10 Myrs as seen for the evolution of one clone in Fig. S3 (B).

While the present precision of the orbit of 2020 AV₂ prevents predicting its orbital behavior on timescales exceeding a few 10 Myrs, it is apparent from its orbital evolution that it is a transitory inhabitant of the inner Venus region of the Solar System. The majority of orbital clones have several lunar distances encounters with Venus and the Earth within 10-20 Myr that have the effect of exciting their orbits onto trajectories crossing with the orbit of Jupiter. The crossing of the orbit of Jupiter has the effect of exciting test particles' orbits onto hyperbolic trajectories after a close encounter with the giant planet sending them out of the Solar System as seen for one of the orbital clones in Fig. S3 (C). The majority of the clones are ejected from the Solar System during close encounters with Jupiter after ~ 20 Myr consistent with the mean ~ 10 Myr lifetimes of near-Earth objects originating from the Main Belt (5, 17) and independent

integrations by Greenstreet 2020.

Comparison with the NEA population: One of the dynamical pathways for inner-Venus asteroids is to originate from the Main Asteroid belt through source regions located near various major planetary resonances (42). If we assume that 2020 AV₂ originated from the Main Belt as an asteroid family fragment (43) before crossing inside of the orbit of Venus, asteroids with orbits similar to 2020 AV₂ according to the Granvik et al. (2018) NEA model most likely originate with a $\sim 77\%$ probability from the ν_6 resonance that forms the boundary of the inner Main Belt at 2.2 au (44). The second most likely source of 2020 AV₂ with a $\sim 18\%$ probability are the Hungaria asteroid population located just exterior to the Main Belt at 2.0 au (45) and the third most likely at $\sim 4\%$ being the 3:1 mean motion resonance with Jupiter located in the Main Belt at 2.5 au (46).

Given its dynamical preference for originating from the inner Main belt, it is no surprise that 2020 AV₂ has a S-type spectrum as seen in Fig. 3 since the majority of asteroids located in the inner Main Belt have spectra similar to S-types (13). We can take the spectral and dynamical classification one step further by comparing its source region probability with the NEA albedo model of Morbidelli et al. (2020) to estimate its surface reflectivity as an independent constraint on its spectral type. Comparing our source region probabilities with the NEA albedo model, it is likely that 2020 AV₂ has an albedo of ~ 0.2 , consistent with the typical albedo for S-type asteroids (15). Combining our albedo estimate from the NEA albedo model with our estimate of the absolute magnitude of $H = 16.4 \pm 0.8$ for 2020 AV₂ in the $H-G$ system (47) from our determination of its orbit, we measure a diameter of $\sim 1.5 \pm 0.5$ km making it one of the rare remaining undiscovered km-scale NEAs (5). Our uncertainties on the diameter of 2020 AV₂ are conservatively estimated by assuming a $1-\sigma$ uncertainty of ~ 0.7 , which is greater than the ~ 0.3 magnitudes scatter on H of asteroids from the Minor Planet Center catalog (48), roughly taking into account the uncertainty caused by the unknown phase function of 2020 AV₂ and the

large $\sim 100^\circ$ phase angle the asteroid was observed at in 2020 January (49). In addition, the NEA model predicts that there are $\sim 1,100$ asteroids in the absolute magnitude range between $15 < H < 18$ of which $\sim 0.22\%$ or ~ 2 are inner-Venus asteroids (5). This number of inner-Venus asteroids predicted by the NEA model shrinks to $0.29 \pm_{0.24}^{0.57}$ when we only consider asteroids brighter than in the $1-\sigma$ range of the H of 2020 AV₂, $< H = 16.4 \pm 0.8$.

Estimating the ZTF inner-Venus asteroid population completeness: We generate a synthetic population of inner-Venus asteroids to compare with our discovery of 2020 AV₂ with the predicted inner-Venus asteroid population from the NEA model (5). We oversample a medium resolution version of the NEA model with $da = 0.05$ au, $de = 0.02$, $di = 2.0^\circ$, $dH = 0.25$ by a factor of 1,000 generating 1,168,279 asteroids with $15 < H < 18$ of which 2,521 are inner-Venus asteroids by definition with an aphelion distance < 0.718 au. The a , e , i and H distributions of our synthetically generated inner-Venus asteroids from the NEA population models are plotted in Fig. 4 (A-D).

To simulate the discovery and observations of our synthetic inner-Venus asteroids by ZTF, we use the complete list of ZTF telescope pointings used during the Twilight Survey between 2019 September 20 UTC and 2020 January 30 UTC plotted in Fig. S2 with a survey simulator (50). We took into account trailing-losses on objects' apparent brightnesses in the survey simulation. The output of the survey simulator produces a list of synthetic inner-Venus asteroids detections from the survey simulation that can be used to roughly estimate the completeness of the ZTF survey in detecting inner-Venus asteroids. We refine our synthetic inner-Venus asteroid observation estimates by calculating completeness for each synthetic inner-Venus asteroid detection in each field. The per object per field completeness is estimated by comparing actual detections of known moving objects serendipitously observed in the Twilight Survey fields with the predicted number of known objects detected in the fields. The Twilight Survey per object

completeness as a function of V magnitude is presented in Fig. S4 (C). A function of the form

$$\epsilon(V) = \epsilon_0 \left[1 + \frac{V - V_{lim}}{V_{width}} \right]^{-1} \quad (1)$$

is used to interpolate the per-field completeness with $\epsilon_0 = 0.87$ representing the maximum possible completeness for detecting moving objects, $V_{lim} = 20.60$ mag, representing the limiting magnitude of the survey where the completeness drops to half for detecting moving objects and $V_{width} = 0.74$ representing the width of the transition in the drop of the completeness in detection faint moving objects (49) and is plotted as a red line in Fig. S4 (C). We note that the value of $\epsilon_0 = 0.87$ is remarkably close to the fill factor of ZTF (7) suggesting that the limiting factor in detecting bright moving objects by ZTF is the detector layout rather than the ZTF processing pipeline (26). In addition to the limiting magnitude, trailing losses due to the sky plane motion of the inner-Venus asteroids could further decrease the completeness calculated with Eq. (1) (49). However, as seen in Fig. S4 (B), the vast majority of synthetic inner-Venus asteroid detections have a sky plane rate of motion of 1.6 degrees/day or slower which doesn't result in significant trailing of the detections given the typical 2 arcseconds seeing at the Palomar observing site. The lack of preference for slower-moving objects seen in the rate of motion distribution of the detected number of objects plotted in red in Fig. S4 (B) compared to the rate of motion distribution of synthetic inner-Venus asteroids suggests that losses due to trailing within the inner-Venus asteroid population are negligible.

The per inner-Venus asteroid, j , per session, n , completeness, $\epsilon_{j,n}(V_{j,n})$ is given by its per session field visible magnitude, $V_{j,n}$ using equation Eq. (1). If a synthetic inner-Venus asteroid is not seen >3 times or not seen at all during a given session n , $\epsilon_{j,n}(V_{j,n}) = 0$. The vast majority of synthetic inner-Venus asteroids have V magnitude <20 as seen in Fig. S4 (A) resulting in the majority of inner-Venus asteroid detections located in Twilight Survey fields having $\epsilon_{j,n}(V_{j,n}) > 70\%$.

The probability of detecting a single Synthetic inner-Venus asteroid, j , p_j , over the total n_{max} Twilight Survey sessions is given by the following equation

$$p_j = 1 - \prod_{n=0}^{n_{max}} [1 - \epsilon_{j,n}(V_{j,n})] \quad (2)$$

where $n_{max} = 89$ corresponding to 90 individual Twilight Survey sessions. The number of detected synthetic inner-Venus asteroids is weighted per synthetic inner-Venus asteroid a , e , i and H bin by each detected object's p_j . The completeness of synthetic inner-Venus asteroids detected by the synthetic ZTF survey per synthetic inner-Venus asteroid a , e , i and H bin is calculated by dividing the weighted number of synthetic inner-Venus asteroids detected per synthetic inner-Venus asteroid a , e , i and H bin by the total number of synthetic inner-Venus asteroids generated from the NEA model per synthetic inner-Venus asteroid a , e , i and H bin. The completeness of inner-Venus asteroids detected per a , e , i and H bin is plotted with a red line in Fig. 4 (A-D). Marginalizing over the complete a , e , i and H distribution of the synthetic inner-Venus asteroid population results in an integrated completeness of ~ 0.15 and a completeness of ~ 0.18 when considering inner-Venus asteroids within a 68.2% confidence interval encompassing 2020 AV₂'s H magnitude.

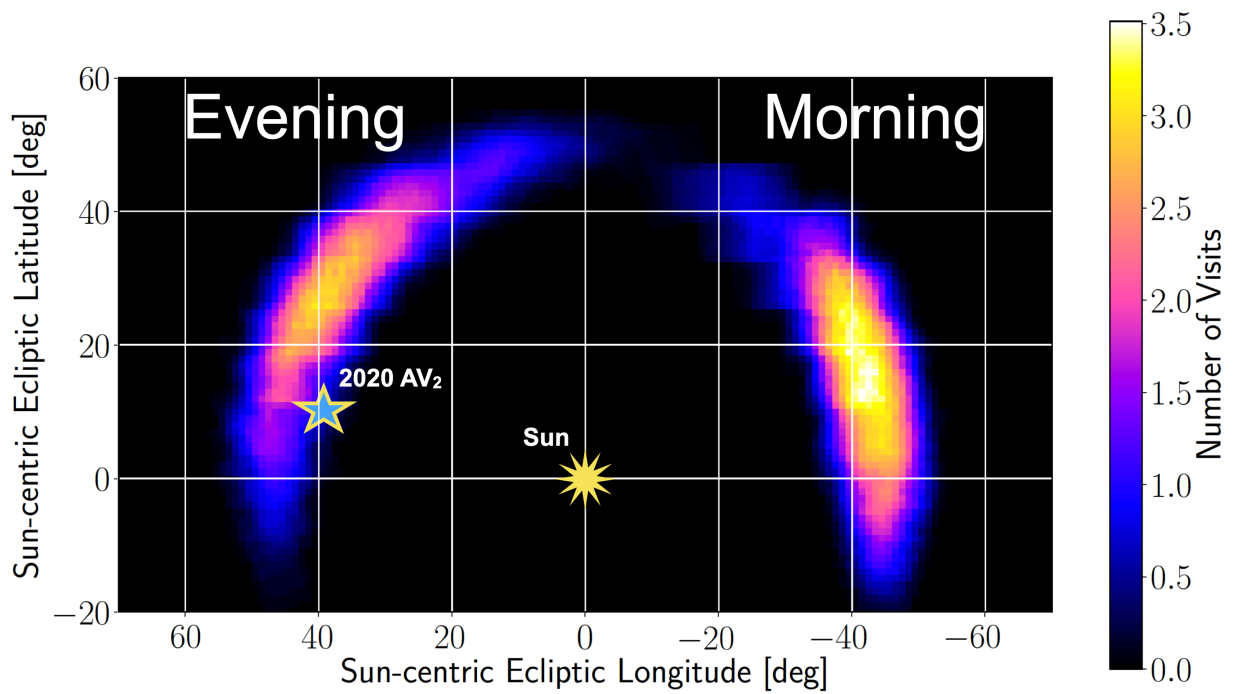


Figure S1: Skyplane distribution of Twilight Survey coverage occurring between 2019 September 19 UTC and 2020 January 30 UTC. The star plots the discovery locations of inner-Venus asteroid 2020 AV₂. The color scale is the number of ZTF visits per square degree as a function of ecliptic longitude and latitude.

Table S1: Orbital elements of 2020 AV₂ based on observations collected between 2020 January 4-23 UTC. The orbital elements are shown for the Julian date (JD) shown using the software Find_Orb by Bill Gray. The 1- σ uncertainties are given in parentheses. The value and 1- σ uncertainties for H is provided by the JPL Small-Body Database Browser entry for 2020 AV₂.

Element	
Epoch (JD)	2,458,871.5
Time of perihelion, T_p (JD)	2,458,907.045 \pm (0.019)
Semi-major axis, a (au)	0.55536 \pm (8.51 \times 10 ⁻⁵)
Eccentricity, e	0.177296 \pm (0.000222)
Perihelion, q (au)	0.456893 \pm (0.000192)
Aphelion, Q (au)	0.653817 \pm (0.000825)
Inclination, i ($^\circ$)	15.880 \pm (0.006)
Ascending node, Ω ($^\circ$)	6.7065 \pm (0.0032)
Argument of perihelion, ω ($^\circ$)	187.305 \pm (0.017)
Mean Anomaly, M ($^\circ$)	275.350 \pm (0.019)
Absolute Magnitude, H	16.4 \pm (0.8)

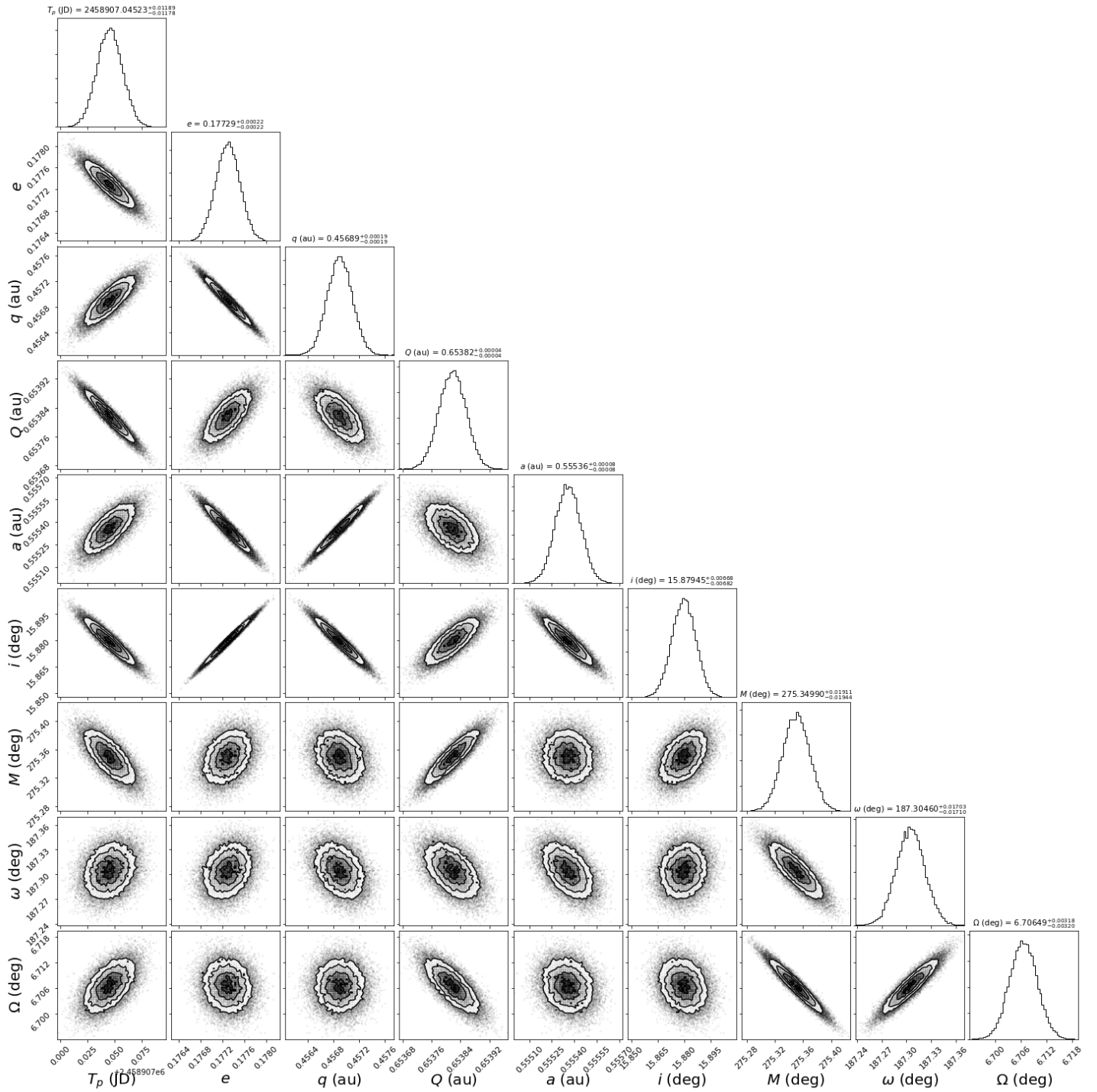


Figure S2: Corner plot of 30,000 samples from the multivariate distribution of orbital elements of 2020 AV₂ from the covariance obtained with the orbit fit from observations between 2020 January 4-23 UTC. The central value and the 1- σ uncertainty for each parameter value is given at the top of each column in the corner plot.

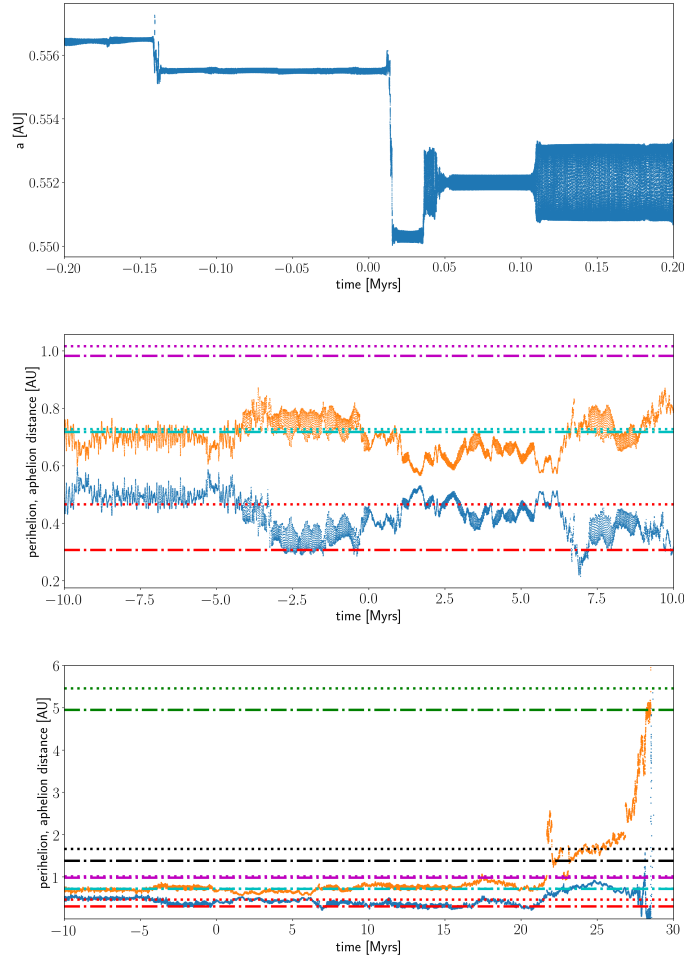


Figure S3: (A) Evolution of the semi-major axis of 2020 AV₂. The plateaus in the evolution of the semi-major axis separated by jumps are due to 2020 AV₂ crossing resonances with Venus and Jupiter. At around 0.05 Myrs, 2020 AV₂ entered a 3:2 mean motion resonance with Venus that lasts for a few 0.1 Myrs. (B) The evolution of the aphelion (orange) and perihelion (blue) distances of 2020 AV₂ integrated to ± 10 Myrs. The current aphelion (dashed line) and perihelion distances (dash-dot line) are plotted as horizontal lines for Venus (cyan) and Mercury (red) and Earth (purple). The aphelion distance of 2020 AV₂ spends the majority of the simulation within the perihelion distance of Venus (0.718 au) and the perihelion distance less than the aphelion distance of Mercury (0.467 au) for most of the simulation and crosses Mercury's perihelion distance (0.307 au) at 6 Myrs during the simulation having a perihelion of ~ 0.25 au. (C) The same as the top panel, except extending the orbital evolution to 30 Myrs. The aphelion (dashed line) and perihelion distances (dash-dot line) are plotted as horizontal lines for Mars (black) and Jupiter (green). A close encounter with the Earth of ~ 0.01 au at ~ 22 Myrs and subsequent perturbations from the other planets results in 2020 AV₂ eventually increasing in its aphelion distance until it encounters Jupiter and is ejected from the Solar System at ~ 28 Myrs. The majority of the clones of 2020 AV₂ are lost in a similar manner after 10-20 Myrs.

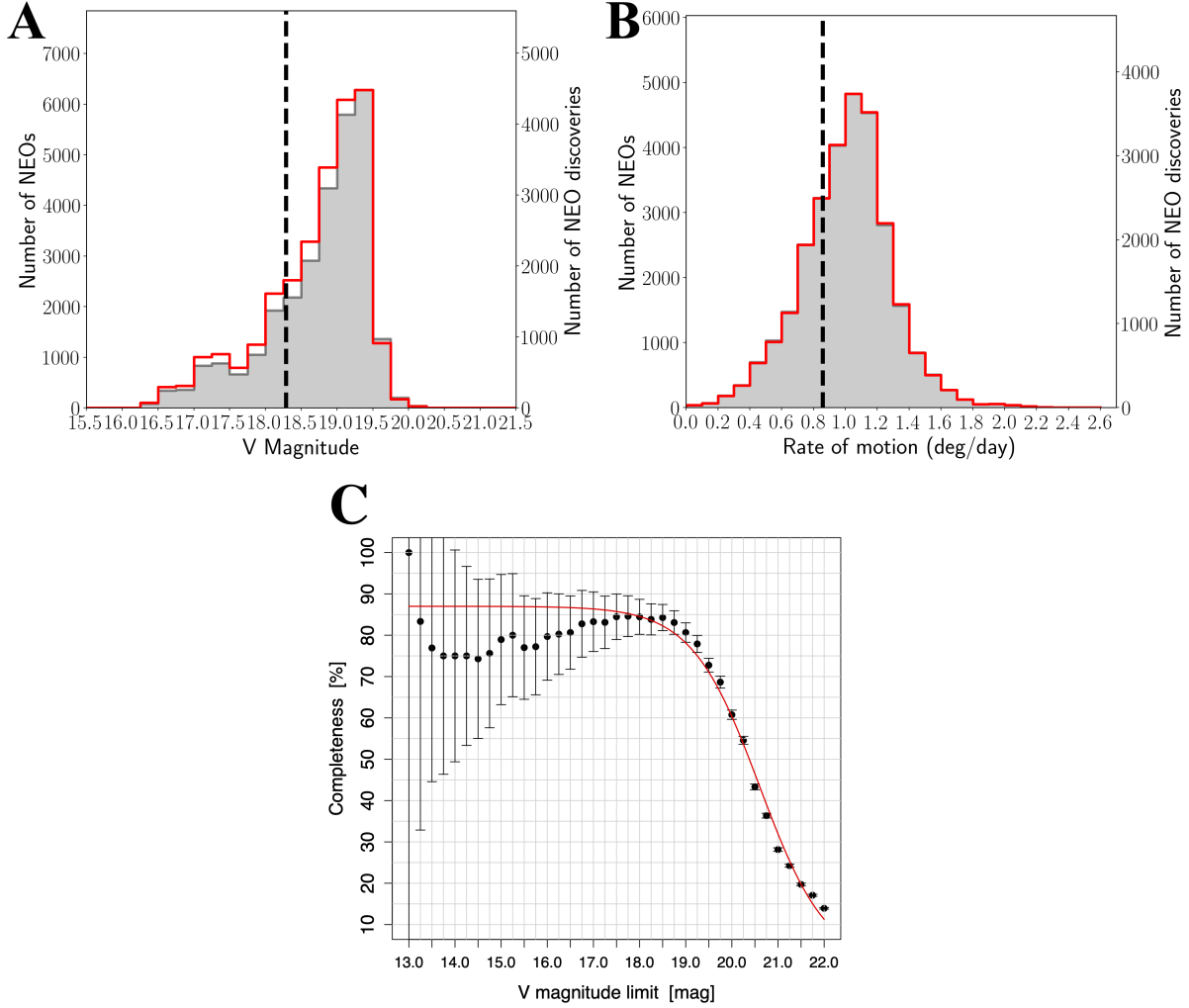


Figure S4: (A) Comparison of the synthetic inner-Venus asteroid apparent V magnitude distribution with the weighted V magnitude distribution of detected inner-Venus asteroids in the survey simulation. Detections are weighted using Eqs. (1) and (2). (B) Same as (A), but for the synthetic inner-Venus asteroid's rate of motion. The vertical dashed lines in (A) and (B) are the values of the apparent V magnitude and rate of motion of 2020 AV₂ on 2020 January 4 UTC. (C) Detection efficiency as a function of V magnitude. The 1- σ error bars are determined assuming Poissonian statistics. Eq. (1) using $\epsilon_0 = 0.87$, $V_{lim} = 20.60$, $V_{width} = 0.74$ is plotted in red.